The influence of mixed-phase clouds on surface shortwave irradiance during the Arctic spring

Dan Lubin[1] and Andrew M. Vogelmann[2]

[1]   The influence of mixed-phase stratiform clouds on the surface shortwave irradiance is examined using unique spectral shortwave irradiance measurements made during the Indirect and Semi-Direct Aerosol Campaign (ISDAC), supported by the U.S. Department of Energy Atmospheric Radiation Measurement (ARM) program. An Analytical Spectral Devices (ASD, Inc.) spectroradiometer measured downwelling spectral irradiance from 350 to 2200 nm in one-minute averages throughout April–May 2008 from the ARM Climate Research Facility's North Slope of Alaska (NSA) site at Barrow. This study examines spectral irradiance measurements made under single-layer, overcast cloud decks having geometric thickness < 3000 m. Cloud optical depth is retrieved from irradiance in the interval 1022–1033 nm. The contrasting surface radiative influences of mixed-phase clouds and liquid-water clouds are discerned using irradiances in the 1.6-μm window. Compared with liquid-water clouds, mixed-phase clouds during the Arctic spring cause a greater reduction of shortwave irradiance at the surface. At fixed conservative-scattering optical depth (constant optical depth for wavelengths $\lambda < 1100$ nm), the presence of ice water in cloud reduces the near-IR surface irradiance by an additional several watts-per-meter-squared. This additional reduction, or supplemental ice absorption, is typically ~5 W m^{-2} near solar noon over Barrow, and decreases with increasing solar zenith angle. However, for some cloud decks this additional absorption can be as large as 8–10 W m^{-2}.

Citation: Lubin, D., and A. M. Vogelmann (2011), The influence of mixed-phase clouds on surface shortwave irradiance during the Arctic spring, *J. Geophys. Res.*, *116*, D00T05, doi:10.1029/2011JD015761.

1.   Introduction

[2] The Indirect and Semi-Direct Aerosol Campaign (ISDAC) of April 2008, supported by the U.S. Department of Energy Atmospheric Radiation Measurement (ARM) and Atmospheric Science programs, provided a new data set on microphysical processes of clouds and aerosols for the springtime Arctic that is unprecedented in its completeness and sophistication. A Convair 580 research aircraft operated by the National Research Council of Canada, flew 27 successful sorties in a single month, carrying 42 separate instruments sampling atmospheric dynamics, cloud microphysics, and aerosol microphysics and chemistry [*McFarquhar et al.*, 2011]. Many of these aircraft measurements could be colocated and intercompared with continuous radiometric and remote sensing data provided by the ARM Climate Research Facility's North Slope of Alaska (NSA) site at Barrow, Alaska [*Stamnes et al.*, 1999].

[3] One major goal of ISDAC was to foster improvements in the parameterization and simulation of mixed-phase clouds [e.g., *Fridlind et al.*, 2007; *Gettelman et al.*, 2010]. In turn, a prime motivation for better understanding of mixed-phase cloud microphysics is to understand how the frequently Arctic stratiform mixed-phase clouds regulate shortwave radiation at the surface and influence sea ice and the ice-albedo feedback [*Perovich et al.*, 2008]. We therefore participated in ISDAC by deploying a shortwave spectroradiometer at the NSA site. Using spectral measurement of shortwave surface downwelling irradiance at both visible and near-infrared (near-IR) wavelengths, we hope to quantify the contrasting roles of liquid water and ice in governing cloud optical properties, where these roles are ultimately related to differences between the complex refractive indices of water versus ice.

[4] Our springtime deployment of a shortwave (visible plus near-IR) spectroradiometer is an example of new spectroscopic techniques being applied to the study of Arctic clouds, aerosols, and climate [e.g., *Ehrlich et al.*, 2008; *Grenfell and Perovich*, 2008; *McBride et al.*, 2011], and high altitude ice clouds in the tropics [e.g., *Baran and Labonnote*, 2007; *Kindel et al.*, 2010]. In a program most similar to ours, *Grenfell and Perovich* [2008] deployed a very similar instrument on a summer-autumn Arctic Ocean

---

[1]Scripps Institution of Oceanography, University of California, San Diego, La Jolla, California, USA.
[2]Brookhaven National Laboratory, Upton, New York, USA.

crossing by the U.S. Coast Guard Cutter *Healy*. Their data provide valuable insights into cloud and sea-ice interactions with shortwave radiation. Regarding long-term observations, the U.S. National Science Foundation has maintained a spectroradiometer covering ultraviolet and visible wavelengths at Barrow since 1991 [*Bernhard et al.*, 2007]. This data set has proven useful for determining ozone variability, atmospheric transmission, aerosol attenuation, and cloud optical depth at conservative-scattering wavelengths; however, it does not provide coverage out to near-IR wavelengths that contain information about cloud microphysical properties. The broadband (pyranometer) shortwave measurements from the NSA have proven useful for estimating climatological cloud properties such as optical depth and shortwave transmittance [e.g., *Dong and Mace*, 2003; *Lubin and Vogelmann*, 2010]; but again, these measurements contain no direct shortwave information about cloud phase and particle size.

[5] Stratiform clouds are a major climatological feature of the springtime Arctic [*Intrieri et al.*, 2002], which commonly exhibit mixed-phase properties [e.g., *Hobbs and Rangno*, 1998; *Shupe et al.*, 2006]. Our objective here is to investigate the influence of ice-water content on the radiative properties of stratiform clouds during the Arctic spring. The spectral shortwave irradiance measurements allow us to determine when and to what magnitude the cloud ice alters the reduction of surface shortwave radiation, as compared with liquid-water clouds.

2. Data

[6] The Analytical Spectral Devices (ASD, Inc.) FieldSpec ProJR spectroradiometer consists of three spectrometer-detector modules that together cover the wavelength range 350–2500 nm. The instrument was enclosed in a temperature-controlled housing on top of the NSA guest facility building. Data collection was continuous from 01 April to 31 May, 2008; the only interruptions being approximately five minutes each morning for instrument hygiene checks and data backup. To measure downwelling spectral irradiance, the instrument was fitted with a radiometric cosine receptor (RCR) that is transparent out to 2200 nm. Thus, some of the 2.2-μm window is not covered, but enough of this window is sampled to provide useful cloud microphysical information. The RCR is a transmitting diffuser type, with no external dome. It is mounted directly on the weatherized instrument housing, and connected to the spectroradiometer by fiber-optic cable. Heating elements within the housing warmed the RCR sufficiently to prevent ice or frost buildup during all but the most severe precipitation events (in these cases, NSA station personnel cleaned the instrument and kept maintenance records). With cosine receptors of this type, angular response is a potential source of error. According to information provided by the manufacturer, the RCR's deviation from perfect cosine angular response in the spectral interval 400–1000 nm increases linearly from zero at overhead illumination to approximately +10% at 60° illumination angle, then decreases to zero for larger illumination angles up to 76°. At 1600 nm, RCR angular performance is better, with cosine error < +2% for illumination angles 0–60°, with degraded performance to an error of −10% by illumination angle 76°. *Meywerk and Ramanathan* [1999] evaluated the performance

of a similar diffusing cosine receptor, and found that this type of cosine response required corrections for clear-sky irradiance (i.e., with prominent direct beam solar illumination) of −0.3% for overhead sun up to −10.5% for solar zenith angle $\theta_o = 60°$. In this study, we are considering only diffuse radiation under overcast skies, and no attempt is made to derive a correction for RCR cosine angular response deviation.

[7] The instrument's spectral resolution is approximately 3 nm between 350 and 1000 nm, and 10 nm between 1000 and 2200 nm. The spectrometer modules utilize linear detector arrays (a Si photodiode array for 350–1000 nm; two InGaAs arrays covering 1000–2500 nm) so that scanning time is a very rapid 100 ms. Therefore, spectral irradiance data could be recorded in one minute averages throughout the field program. In consultation with the ISDAC Science Team when planning the field campaign, no justification was found for higher time resolution sampling, and the one-minute averaging was adopted to keep the data volume manageable. The field deployment was short enough that pre- and post-season instrument checkups and recalibration by the manufacturer were adequate to establish NIST-traceable radiometric calibration. These ISDAC spectroradiometer data have been placed in the ARM archive, along with a report on the calibration procedure.

[8] To interpret these irradiance spectra, we utilize three supporting data sets from NSA. The first is the Active Remotely Sensed Cloud Locations (ARSCL) data set [*Clothiaux et al.*, 2000], which provides high-time-resolution masks of cloud layering and altitude through a synthesis of lidar and radar data, with range gates having vertical resolution 45 m. The second is the Total Sky Imager (TSI) data set, from which we identify overcast sky conditions. The third is the set of twice-daily rawinsonde observations launched from NSA. Using ARSCL, we identify scenes containing only a single cloud layer having thickness between 45 and 3000 m and cloud base < 1000 m. Thicker single-layer cloud decks appear in the ARSCL data set, but it is possible that these cases comprise multiple cloud layers with precipitation in between. We label a scene as overcast if the TSI cloud fraction is ≥95% in the 160° field of view, and ≥97% in the 100° field of view. The complementary criteria on horizontal cloud fraction (TSI) and single-layered vertical cloud structure (ARSCL) should serve to obtain relatively uniform cloud systems for our analysis. Cloud temperature is evaluated as the average of the sonde temperature measurements over the altitude range between the cloud base and cloud top given by ARSCL. We therefore analyze only the spectral irradiance data obtained under overcast skies having single-layer clouds <3000 m thick.

3. Evaluating Mixed-Phase Supplemental Ice Absorption

[9] We wish to determine how frequently solar radiation attenuation by single-layer stratiform clouds over Barrow during April–May 2008 was influenced by mixed-phase properties. To do so, we calculate a supplemental ice absorption, A_{si}, for each measured irradiance spectrum. The theoretical basis is illustrated in Figures 1 and 2. These calculations use a discrete-ordinates-based (DISORT) radiative transfer model [*Lubin and Vogelmann*, 2007; *Stamnes*
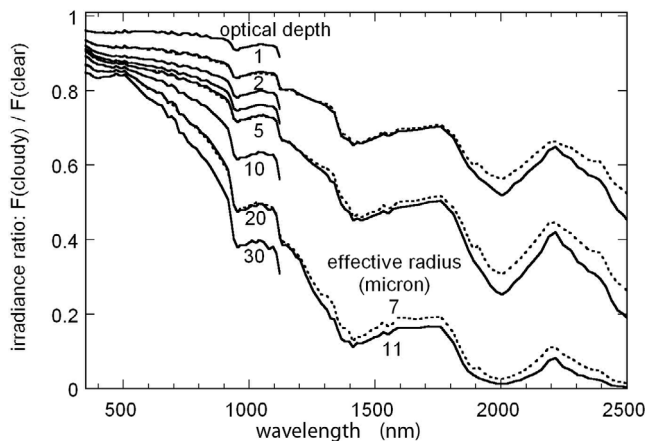
Figure 1. DISORT simulation of the spectral dependence of liquid-water cloud attenuation of surface shortwave irradiance (relative to clear sky) as a function of cloud optical depth. The surface albedo is that of new snow, and the solar zenith angle 60°. For clarity, only the curves for optical depths 2, 5, and 20 are fully shown. Solid and dotted curves depict the flux ratio for droplet effective radius 11 and 7 μm, respectively.

et al., 1988] with background aerosol attenuation, and with a spectral surface albedo for new snow [*Perovich et al.*, 2002] that was previously found to be representative of Barrow throughout April and May [*Lubin and Vogelmann*, 2010]. In situ spectral surface albedo measurements made by *Lyapustin et al.* [2010] near Barrow during April 2008 confirm that the spectral albedo of new snow is appropriate. In addition, we examined NSA measurements of broadband surface albedo for April and May 2008, and found that the surface albedo remains high and approximately constant with time for the purposes of this study.

[10] Figure 1 shows how the spectral surface downwelling irradiance varies over new snow as a function of cloud optical depth, τ_c, for liquid-water clouds having effective droplet radii, r_e, of 11 μm and 7 μm, which are representative of clean-air and aerosol-activated Arctic stratus clouds, respectively [*Lubin and Vogelmann*, 2006; *Garrett and Zhao*, 2006]. In evaluating the droplet size distribution, we use a lognormal form with effective variance of 0.27, which is found by *Garrett and Zhao* [2006] to be representative of Arctic clouds. In the visible portion of the spectrum (e.g., <600 nm), the high surface albedo (0.98) causes substantial multiple reflection of photons between the surface and cloud base, yielding a weak dependence of surface irradiance on cloud optical depth. At the slightly longer wavelengths of 1022–1033 nm, the albedo of the new snow surface is substantially lower (0.72), yielding a greater sensitivity in surface irradiance to cloud optical depth. At fixed cloud optical depth, the difference in surface spectral irradiance between the $r_e = 11$ μm and $r_e = 7$ μm cases is very small, becoming noticeable (~13% in irradiance by 1500 nm) for cloud optical depths 20 and higher. This is due to a small difference in the near-IR single-scattering albedo between these two liquid-water cloud cases. For example, at 1553 nm the single-scattering albedos are 0.98925 and 0.99312 for the $r_e = 11$ μm and $r_e = 7$ μm cases, respectively.

[11] At conservative scattering wavelengths ($\lambda < 1100$ nm; negligible absorption by hydrometeors) it makes essentially no difference when retrieving τ_c whether the cloud is liquid water, ice, or mixed-phase. For example, at 1028 nm the single-scattering albedos for the $r_e = 11$ μm and $r_e = 7$ μm liquid-water clouds are 0.99939 and 0.99983, respectively, while the single-scattering albedos for ice clouds having effective particle sizes of 10, 30, and 50 μm are 0.99972, 0.99925, and 0.99876, respectively. Thus, the differences in single-scattering albedo for these five cases at 1028 nm are an order of magnitude smaller than the differences between the two liquid-water cloud cases at 1553 nm that gave rise to the small surface irradiances differences shown in Figure 1.

[12] Figure 2 shows that in the near-IR windows the difference between liquid-water and ice refractive indices is strongly manifested, even when the conservative-scattering τ_c is held constant. For example, at 1553 nm the single-scattering albedos for ice clouds having effective particle sizes 10, 30, and 50 μm are 0.97088, 0.92284, and 0.88141, respectively, in contrast to the single-scattering albedo of 0.98925 for the $r_e = 11$ μm liquid-water clouds. In the 1.6-μm window, cloud ice water will always cause additional attenuation of surface irradiance, relative to a liquid-water cloud having the same τ_c. This is not always the case in the 2.2-μm window. Ice clouds having larger effective particle size show stronger attenuation than the liquid-water case at fixed τ_c, but for smaller ice particles (~10 μm) the spectral irradiance is very similar to the liquid-water case or even greater.

[13] We therefore calculate the supplemental ice absorption A_{si} in a three-step process. In the first step, we determine the conservative-scattering cloud optical depth, τ_c, that matches the model-calculated surface irradiance with the measured surface irradiance in the 1022–1033 nm wavelength band. In the second step, we calculate a theoretical surface spectral irradiance $F_{T11}(\tau_c, \lambda)$ using that value of τ_c and the same solar-illumination geometry, for a liquid-water cloud having an effective droplet radius of 11 μm. In the third step, we integrate over the 1.6-μm window (1374–1838 nm) both the modeled spectral irradiance
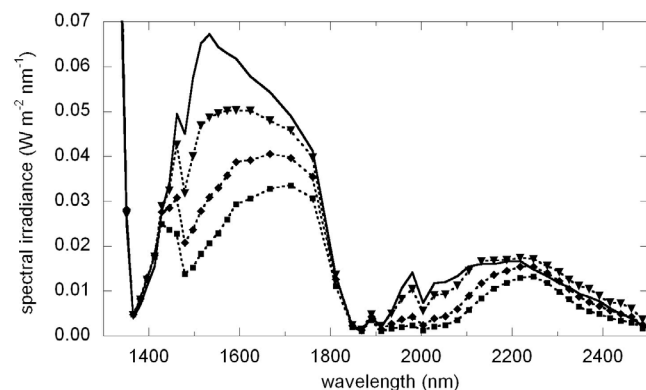
Figure 2. DISORT simulation of downwelling surface spectral irradiance in the 1.6 and 2.2 μm windows. The cloud optical depth (conservative scattering) is 5 over a new snow surface and the solar zenith angle is 60°. The liquid-water cloud has an effective radius 11 μm (solid curve), and the ice cloud has effective particle sizes of 10, 30, and 50 μm (triangles, diamonds, squares, respectively).
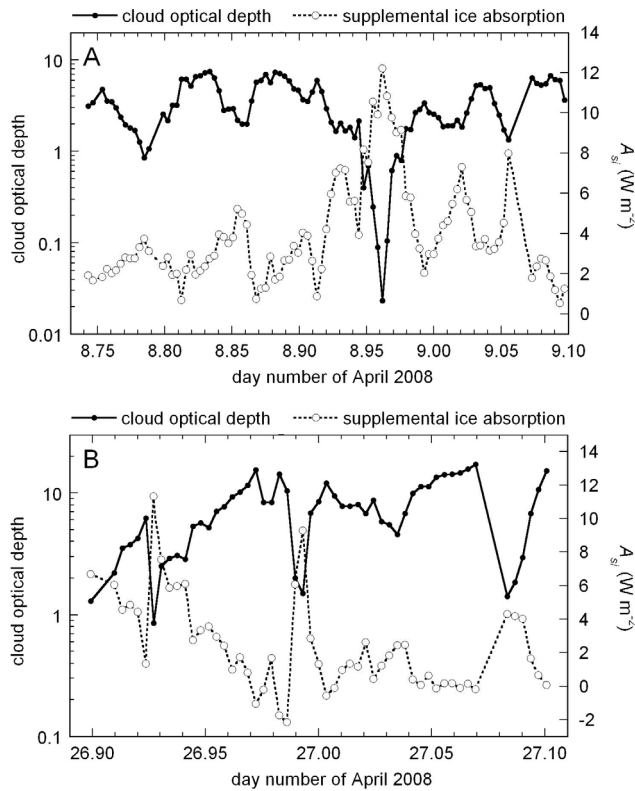
Figure 3. Time series of 5-min-averaged cloud optical depth τ_c and supplemental ice absorption A_{si} in the 1.6-μm window, from the ISDAC "Golden Days" of (a) 8 and (b) 26 April 2008.

under this liquid-water cloud and the measured spectral irradiance $F_M(\lambda)$, and then subtract the measured value from the theoretical liquid-water-cloud value. We define this difference as

$$A_{si} = \int_{1374nm}^{1838nm} F_{T11}(\tau_c, \lambda)d\lambda - \int_{1374nm}^{1838nm} F_M(\lambda)d\lambda,$$

which can be specified in W m^{-2} to directly note the effect of cloud ice water on the surface energy budget for a specific instance. Alternatively, A_{si} could be specified in percent (relative to the theoretical liquid-water-cloud value) if one wishes to survey the entire data set and draw conclusions that are not influenced by solar zenith angle dependencies.

[14] To summarize, retrieving τ_c in the wavelength interval 1022–1033 nm utilizes an even more transparent part of the spectrum than at most visible wavelengths (i.e., smaller Rayleigh scattering, no ozone absorption, and negligible water vapor absorption), and also takes advantage of a lower snow surface albedo (0.72 versus 0.98), while still working in a conservative-scattering regime for cloud attenuation (i.e., negligible absorption by the cloud particles). Evaluating the supplemental ice absorption A_{si} in the 1.6-μm window, relative to a clean-air liquid-water cloud of the same conservative-scattering τ_c, will always yield $A_{si} > 0$ when ice is present in the cloud. We choose the $r_e = 11$ μm cloud for the liquid-water reference case.

During the Arctic spring, clouds may often experience aerosol activation and have smaller r_e. However, Figure 1 shows that in the near-IR windows at fixed τ_c a smaller r_e results in slightly less attenuation of the surface irradiance, not more. This means only that our procedure for evaluating A_{si} might slightly overstate the influence of cloud-ice water on the surface irradiance if aerosol activation of the liquid-water droplets is present. Failure to account for an aerosol indirect effect (i.e., $r_e < 11$ μm) cannot yield a spurious detection of supplemental ice absorption if only liquid water is present; instead, A_{si} would be slightly negative. Again, this is true because we hold the optical depth τ_c fixed in order to distinguish liquid-water cloud from mixed-phase cloud attenuation. If we wish to examine aerosol indirect effects in liquid-water clouds, we would instead hold the cloud liquid-water path fixed. We note that an actual effective radius $r_e > 11$ μm could yield a spurious detection of positive A_{si}.

[15] Finally, we note that the definition of A_{si} offers the simplicity of not requiring explicit radiative transfer calculations for ice particles. Generally speaking, ice particle shape and habit are important considerations when evaluating the radiative properties of ice clouds, especially for reflected radiances; although equivalent spheres (as used in Figure 2) have validity for transmitted irradiances [*Grenfell and Warren*, 1999; *Neshyba et al.*, 2003] and in the near-IR [e.g., *Mitchell et al.*, 2011]. When evaluating the supplemental ice absorption, we only need to reference radiative transfer simulations for idealized clean-air, liquid-water clouds, for which Mie theory provides an acceptable representation.

4. Results

[16] Figure 3 shows time series of our retrieved τ_c (from the 1022–1033 nm irradiance) and A_{si} (in the 1.6-μm window, integrated over 1374–1838 nm), in five-minute averages, for the two ISDAC "Golden Days" [*McFarquhar et al.*, 2011]. On these days, single-layer, mixed-phase clouds persisted over Barrow, which proved particularly valuable as case studies for climate model parameterization development. Throughout the daylight period of 8 April, there are large oscillations in both τ_c and A_{si}. This is consistent with the wide variability in vertical velocity observed in this cloud deck by the airborne X-band radar [*McFarquhar et al.*, 2011, Figure 12], which is associated with equally rapid changes in cloud microphysical properties observed from the Convair [*McFarquhar et al.*, 2011, Figure 13]. A_{si} is generally positive on 8 April, sometimes exceeding 8 W m^{-2}, which indicates the strong role of ice absorption in regulating the surface shortwave radiation budget. On 26 April, τ_c is generally larger than on 8 April. However, A_{si}, while mostly positive, remains of order 4 W m^{-2}. This suggests a stronger radiative role for cloud liquid water on 26 April, as compared with 8 April.

[17] Figure 4 provides examples of $F_{T11}(\tau_c, \lambda)$ and $F_M(\lambda)$ that illustrate how spectral liquid water and ice absorption determine A_{si}. Two examples from the ISDAC "Golden Days" are shown in Figures 4a and 4b. In both of these cases $A_{si} = \sim 20\%$. In situ aircraft measurements show that these are both mixed-phase cloud layers. The ice particles cause substantial reduction in the near-IR irradiance reaching the
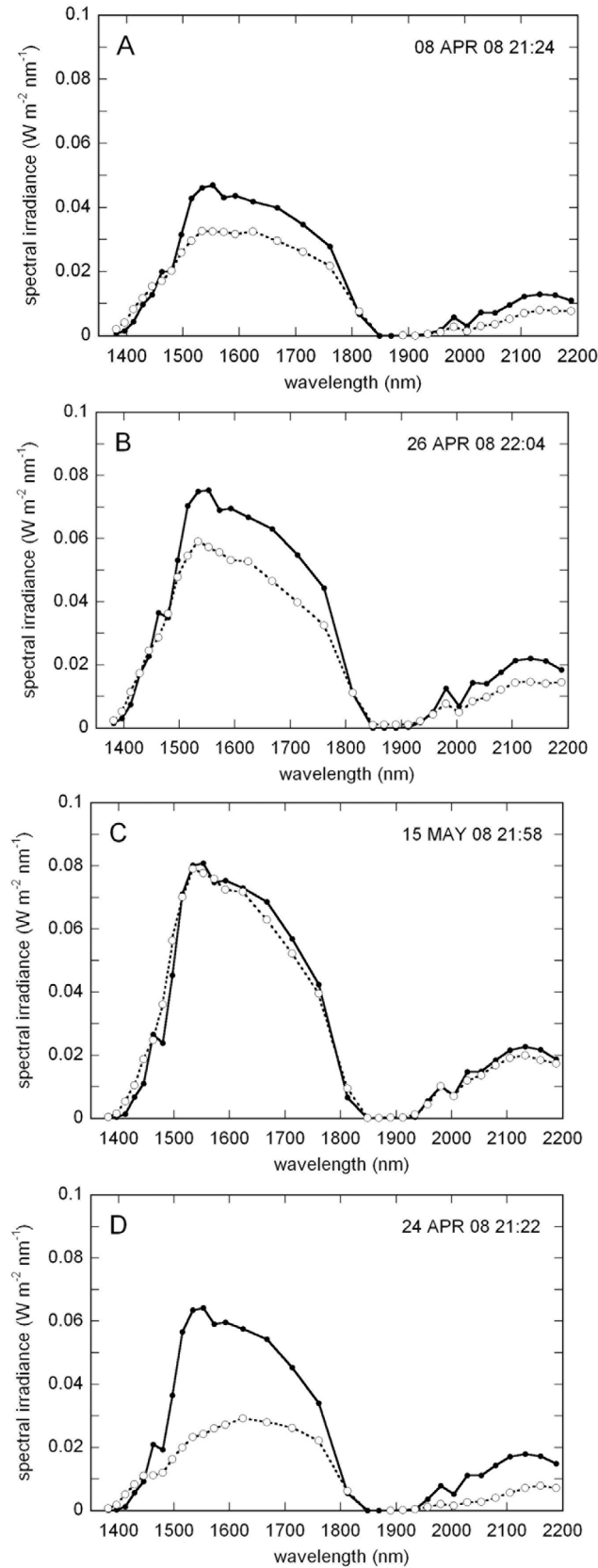
surface in both the 1.6 μm and 2.2-μm windows, but only slightly alter the spectral shape compared with the theoretical liquid water case for the same τ_c. Figure 4c gives an example under a warmer atmosphere in mid-May that is probably mainly a liquid-water cloud. The cloud temperature T_c from the nearest rawinsonde, averaged over the altitude range of the cloud specified by ARSCL, is 269.8 K. In this example there is excellent agreement between $F_{T11}(\tau_c, \lambda)$ and $F_M(\lambda)$. There is some discrepancy at the edge of the 1.6-μm window, in which the radiative transfer model slightly overestimates the water vapor absorption between 1381 and 1515 nm. The discrepancy in this example is 0.62 W m^{-2}, compared with the total irradiance integrated over the 1.6-μm window of 18.4 W m^{-2}. Uncertainty in water vapor absorption at the band edges therefore introduces errors of order 3–4% in detection of A_{si}, which does not affect the conclusions of this study. Figure 4d depicts $F_{T11}(\tau_c, \lambda)$ and $F_M(\lambda)$ in a cloud with considerable influence of ice ($T_c = 259.9$ K and $A_{si} = 47.6\%$). Here the spectral dependence in the measured irradiance is substantially different from the ideal liquid-water cloud case throughout most of the 1.6-μm window.

[18] In practice, we find that most of our A_{si} detections behave in a manner consistent with the examples of Figure 4. However, in a small number of cases the retrieved cloud optical depth τ_c is so large that $A_{si} < -100\%$. It is likely that these retrievals are not physically realistic, with the large τ_c resulting from measurement uncertainty and/or non-plane-parallel radiative transfer effects in the real clouds. Based on the maximum value from the climatology of *Dong and Mace* [2003], we reject from further interpretation all detections for which $\tau_c > 40$. This represents 3.1% of our cases. For the cases we consider physically realistic, 18.3% have $-5\% \leq A_{si} < 5\%$. We interpret these as clouds that are mainly liquid water, which are reasonably well simulated by our radiative transfer model. $A_{si} < -5\%$ occurs in 15.7% of our cases. These may represent liquid-water clouds with $r_e < 11$ μm, or may be artifacts of retrieved τ_c slightly too large (again, due to measurement uncertainty or non-plane-parallel effects). Further work in conjunction with in situ aircraft observations at high time resolution over the NSA site is required to fully understand these cases. For the purposes of this study, we interpret these cases as also representing liquid-water clouds, or at least clouds in which liquid water dominates the attenuation of surface shortwave irradiance. The remaining 55.9% of our cases have $5 \leq A_{si} \leq 53.8\%$. We interpret these as representing mixed-phase clouds in which ice plays a noticeable role in attenuating surface shortwave irradiance.

[19] Figure 4 indicates considerable information in the slope of the spectral irradiance within the 1.6-μm window,

Figure 4. Examples of modeled (solid) and measured (dashed) spectral irradiance, illustrating the behavior of supplemental ice absorption A_{si}; (a) mixed-phase cloud from ISDAC "Golden Day" with $\tau_c = 5.9$, $\theta_o = 64.5°$, $T_c = 260.8$ K, and $A_{si} = 2.7$ W m^{-2} = 20.8%; (b) mixed-phase cloud from ISDAC "Golden Day" with $\tau_c = 4.4$, $\theta_o = 57.5°$, $T_c = 259.9$ K, and $A_{si} = 4.2$ W m^{-2} = 20.2%; (c) liquid-water cloud case with $\tau_c = 5.6$, $\theta_o = 52.3°$, $T_c = 269.8$ K, and $A_{si} = 0$; (d) heavily glaciated cloud with $\tau_c = 5.4$, $\theta_o = 58.9°$, $T_c = 259.9$ K, and $A_{si} = 7.8$ W m^{-2} = 47.6%.
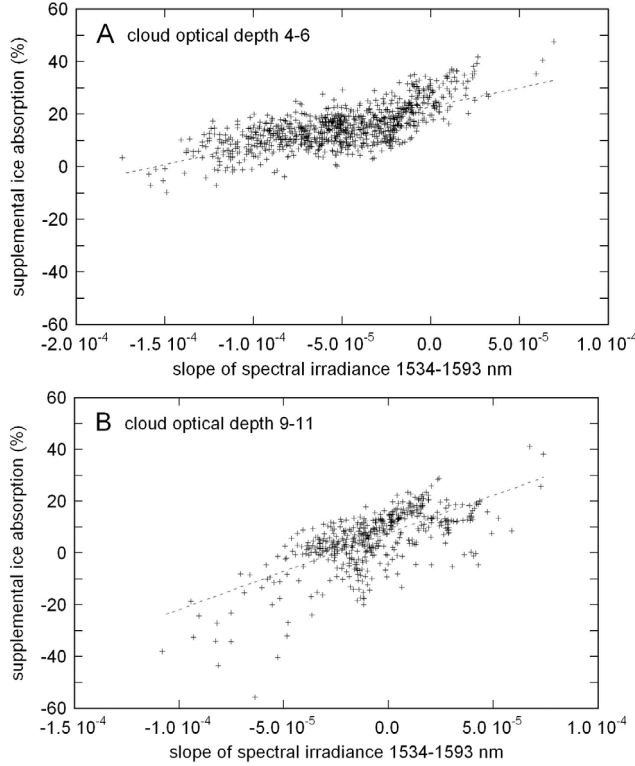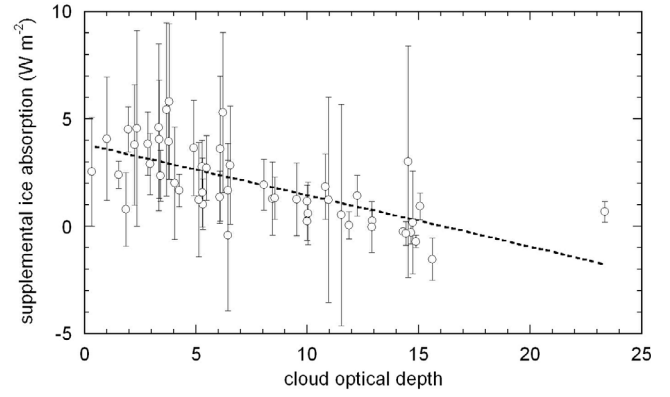
Figure 5. Supplemental ice absorption A_{si} in the 1.6-μm window as a function of the slope of the spectral irradiance across the interval 1534–1593 nm; (a) for all observations with $4 \leq \tau_c \leq 6$; (b) for all observations with $9 \leq \tau_c \leq 11$.

which *McBride et al.* [2011] have used to estimate r_e in liquid-water clouds. The most significant variability occurs over the approximate interval 1530–1600 nm. Here pure liquid water and pure ice water induce slopes of opposite sign. From Figure 2, we can estimate that at $\theta_o = 60°$ and $\tau_c = 5$, the slope of the spectral irradiance in this interval is of order -9×10^{-5} for the liquid-water cloud. This slope varies with both θ_o and τ_c, but is always negative for liquid-water clouds. The presence of ice in various con-
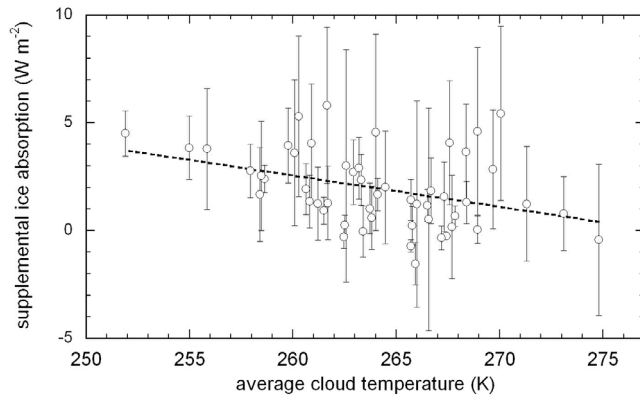
Figure 6. Supplemental ice absorption A_{si} in the 1.6-μm window, averaged over 12-h periods centered on the times of rawinsonde launches, as a function of average cloud temperature T_c from the sonde profiles. Error bars are $\pm 1\sigma$.

Figure 7. Supplemental ice absorption A_{si} in the 1.6-μm window as a function of cloud optical depth τ_c, averaged over the same time periods as in Figure 6. Error bars are $\pm 1\sigma$; horizontal error bars on τ_c have been omitted for clarity.

centrations and particle sizes may make the slope less negative than the pure liquid water case, or may make it positive. In Figure 5, the supplemental ice absorption A_{si} is plotted as a function of the measured slope across the interval 1534–1593 nm, for two small ranges of τ_c. Comparing these with Figure 2, and with the $F_{T11}(\tau_c, \lambda)$ calculations of Figure 4, we see that slopes in this interval of -5×10^{-5} and smaller are associated with A_{si} closer to zero. Flatter and eventually positive slopes are associated with larger and positive A_{si}.

[20] In Figure 6 we show A_{si} as a function of average cloud temperature Tc estimated from the nearest sonde profile. Time averages are over periods as long as 12 h. In Arctic mixed-phase clouds, there is no simple or straightforward relationship between cloud temperature and either ice concentration or ice particle size. Therefore we expect the considerable scatter that appears in this plot. However, there is a noticeable trend in decreasing A_{si} with increasing T_c ($R = 0.37$), with $T_c > 270$ K showing A_{si} close to zero as we would expect for mainly liquid-water clouds. In Figure 7 we show A_{si} plotted against τ_c, both quantities averaged as in Figure 6. There is a decreasing trend in A_{si} with increasing τ_c ($R = 0.68$), which may arise for two reasons. First, our τ_c retrievals show a slight tendency toward larger overall values in May (warmer atmosphere) than in April (colder atmosphere). Second, for stratiform clouds with larger τ_c, liquid water may play a much larger role than ice in governing the surface shortwave irradiance.

5. Conclusions

[21] Compared with liquid-water clouds of the same ($\lambda <$ 1100 nm) optical depth, mixed-phase clouds during the Arctic spring cause a greater reduction of surface shortwave irradiance. This additional reduction, or supplemental ice absorption, is typically ~5 W m^{-2} near solar noon over Barrow, and decreases with increasing solar zenith angle. However, for some cloud decks this additional absorption can be as large as 8–10 W m^{-2}. Both the overall magnitude of the irradiance reduction in the 1.6-μm window (relative to pure liquid-water cloud) and the slope of the spectral

irradiance for wavelengths between ~1530–1600 nm can be used to distinguish between mixed-phased clouds and clouds behaving mainly as liquid-water clouds. The magnitude of the supplemental ice absorption is a complicated function of the partition between cloud liquid and ice water content, the liquid-water droplet size distribution, and the ice-particle size distribution. Further intercomparison of the spectroradiometer data with specific aircraft measurements may help untangle this complexity.

[22] Overall, 34% of our spectral irradiance measurements under single-layer, overcast cloud decks (identified by ARSCL and the TSI) appeared to be consistent with liquid-water clouds, or clouds whose radiative properties are dominated by the liquid phase. The rest of the cases were highly consistent with mixed-phase clouds in which ice particles play a significant role in regulating shortwave radiation at the surface. These surface-spectral-irradiance measurements from ISDAC therefore underscore the importance of mixed-phase cloud properties in understanding the atmospheric energy balance and climate of the high Arctic.

References

Baran, A. J., and L. C. Labonnote (2007), A self-consistent scattering model for cirrus. I: The solar region, *Q. J. R. Meteorol. Soc.*, *133*, 1899–1912, doi:10.1002/qj.164.

Bernhard, G., C. R. Booth, J. C. Ehramjian, R. Stone, and E. G. Dutton (2007), Ultraviolet and visible radiation at Barrow, Alaska: Climatology and influencing factors on the basis of version 2 National Science Foundation network data, *J. Geophys. Res.*, *112*, D09101, doi:10.1029/2006JD007865.

Clothiaux, E. E., T. P. Ackermann, G. G. Mace, K. P. Moran, R. T. Marchand, M. A. Miller, and B. E. Martner (2000), Objective determination of cloud heights and radar reflectivities using a combination of active remote sensors at the ARM CART sites, *J. Appl. Meteorol.*, *39*, 645–665, doi:10.1175/1520-0450(2000)039<0645:ODOCHA>2.0.CO;2.

Dong, X., and G. G. Mace (2003), Arctic stratus cloud properties and radiative forcing derived from ground-based data collected at Barrow, Alaska, *J. Clim.*, *16*, 445–461, doi:10.1175/1520-0442(2003)016<0445:ASCPAR>2.0.CO;2.

Ehrlich, A., E. Bierwirth, M. Wendisch, J.-F. Gayet, G. Mioche, A. Lampert, and J. Heintzenberg (2008), Cloud phase identification of Arctic boundary-layer clouds from airborne spectral reflection measurements: Test of three approaches, *Atmos. Chem. Phys.*, *8*, 7493–7505, doi:10.5194/acp-8-7493-2008.

Fridlind, A. M., A. S. Ackerman, G. McFarqhuar, G. Zhang, M. R. Poellot, P. J. DeMott, A. J. Prenni, and A. J. Heymsfield (2007), Ice properties of single-layer stratocumulus during the Mixed-Phase Arctic Cloud Experiment (M-PACE): 2. Model results, *J. Geophys. Res.*, *112*, D24202, doi:10.1029/2007JD008646.

Garrett, T. J., and C. Zhao (2006), Increased Arctic cloud longwave emissivity associated with pollution from mid-latitudes, *Nature*, *440*, 787–789, doi:10.1038/nature04636.

Gettelman, A., X. Liu, S. J. Ghan, H. Morrison, S. Park, A. J. Conley, S. A. Klein, J. Boyle, D. L. Mitchell, and J.-L. F. Li (2010), Global simulations of ice nucleation and ice supersaturation with an improved cloud scheme in the Community Atmosphere Model, *J. Geophys. Res.*, *115*, D18216, doi:10.1029/2009JD013797.

Grenfell, T. C., and D. K. Perovich (2008), Incident spectral irradiance in the Arctic Basin during the summer and fall, *J. Geophys. Res.*, *113*, D12117, doi:10.1029/2007JD009418.

Grenfell, T. C., and S. G. Warren (1999), Representation of a nonspherical ice particle by a collection of independent spheres for scattering and absorption of radiation, *J. Geophys. Res.*, *104*, 31,697–31,709, doi:10.1029/1999JD900496.

Hobbs, P. V., and A. L. Rangno (1998), Microstructures of low and middle-level clouds over the Beaufort Sea, *Q. J. R. Meteorol. Soc.*, *124*, 2035–2071, doi:10.1002/qj.49712455012.

Intrieri, J., M. D. Shupe, T. Uttal, and B. J. McCarty (2002), An annual cycle of Arctic cloud characteristics observed by radar and lidar at SHEBA, *J. Geophys. Res.*, *107*(C10), 8030, doi:10.1029/2000JC000423.

Kindel, B. C., K. S. Schmidt, P. Pilewskie, B. A. Baum, P. Yang, and S. Platnick (2010), Observations and modeling of ice cloud shortwave spectral albedo during the Tropical Composition, Cloud and Climate Coupling Experiment (TC[4]), *J. Geophys. Res.*, *115*, D00J18, doi:10.1029/2009JD013127.

Lubin, D., and A. M. Vogelmann (2006), A climatologically significant aerosol longwave indirect effect in the Arctic, *Nature*, *439*, 453–456, doi:10.1038/nature04449.

Lubin, D. and A. M. Vogelmann (2007), Expected magnitude of the aerosol shortwave indirect effect in springtime Arctic liquid water clouds, *Geophys. Res. Lett.*, *34*, L11801, doi:10.1029/2006GL028750.

Lubin, D., and A. M. Vogelmann (2010), Observational quantification of a total aerosol indirect effect in the Arctic, *Tellus, Ser. B.*, *62*, 181–189.

Lyapustin, A., et al. (2010), Analysis of snow bidirectional reflectance from ARCTAS Spring-2008 campaign, *Atmos. Chem. Phys.*, *10*, 4359–4375, doi:10.5194/acp-10-4359-2010.

McBride, P. J., K. S. Schmidt, P. Pilewskie, A. S. Kittelman, and D. E. Wolfe (2011), A spectral method for retrieving cloud optical thickness and effective radius from surface-based measurements, *Atmos. Chem. Phys. Discuss.*, *11*, 1053–1104, doi:10.5194/acpd-11-1053-2011.

McFarquhar, G. M., et al. (2011), Indirect and Semi-Direct Aerosol Campaign (ISDAC): The impact of Arctic aerosols on clouds, *Bull. Am. Meteorol. Soc.*, *92*, 183–201, doi:10.1175/2010BAMS2935.1.

Meywerk, J., and V. Ramanathan (1999), Observations of the spectral clear-sky forcing over the tropical Indian Ocean, *J. Geophys. Res.*, *104*, 24,359–24,370, doi:10.1029/1999JD900502.

Mitchell, D. L., R. P. Lawson, and B. Baker (2011), Understanding effective diameter and its application to terrestrial radiation in ice clouds, *Atmos. Chem. Phys.*, *11*, 3417–3429, doi:10.5194/acp-11-3417-2011.

Neshyba, S. P., T. C. Grenfell, and S. G. Warren (2003), Representation of a nonspherical ice particle by a collection of independent spheres for scattering and absorption of radiation: 2. Hexagonal columns and plates, *J. Geophys. Res.*, *108*(D15), 4448, doi:10.1029/2002JD003302.

Perovich, D. K., T. C. Grenfell, B. Light, and P. V. Hobbs, P. V. (2002), Seasonal evolution of the albedo of multiyear Arctic sea ice, *J. Geophys. Res.*, *107*(C10), 8044, doi:10.1029/2000JC000438.

Perovich, D. K., J. A. Richter-Menge, K. F. Jones, and B. Light (2008), Sunlight, water, and ice: Extreme Arctic sea ice melt during the summer of 2007, *Geophys. Res. Lett.*, *35*, L11501, doi:10.1029/2008GL034007.

Shupe, M. D., S. Y. Y. Matrosov, and T. Uttal (2006), Arctic mixed-phase cloud properties derived from surface-based sensors at SHEBA, *J. Atmos. Sci.*, *63*, 697–711, doi:10.1175/JAS3659.1.

Stamnes, K., S.-C. Tsay, W. J. Wiscombe, and K. Jayaweera (1988), Numerically stable algorithm for discrete-ordinate-method radiative transfer in multiple scattering and emitting layered media, *Appl. Opt.*, *27*, 2502–2509, doi:10.1364/AO.27.002502.

Stamnes, K., R. G. Ellingson, J. A. Curry, J. E. Walsh, and B. D. Zak (1999), Review of science issues, deployment strategy, and status for the ARM North Slope of Alaska–Adjacent Arctic Ocean climate research site, *J. Clim.*, *12*, 46–63, doi:10.1175/1520-0442-12.1.46.

D. Lubin, Scripps Institution of Oceanography, University of California, San Diego, 9500 Gilman Dr., La Jolla, CA 92093, USA. (dlubin@ucsd.edu)

A. M. Vogelmann, Brookhaven National Laboratory, Upton, NY 11973, USA.